JACS
JOURNAL OF THE AMERICAN CHEMICAL SOCIETY

# Controlled Self-Assembly of Gold Nanotetrahedra into Quasicrystals and Complex Periodic Supracrystals

Yi Wang, Jun Chen, Ruipeng Li, Alexander Götz, Dominik Drobek, Thomas Przybilla, Sabine Hübner, Philipp Pelz, Lin Yang, Benjamin Apeleo Zubiri, Erdmann Spiecker, Michael Engel,* and Xingchen Ye*

**Cite This:** https://doi.org/10.1021/jacs.3c05299

Read Online

ACCESS | Metrics & More | Article Recommendations | Supporting Information

**ABSTRACT:** The self-assembly of shape-anisotropic nanocrystals into large-scale structures is a versatile and scalable approach to creating multifunctional materials. The tetrahedral geometry is ubiquitous in natural and manmade materials, yet regular tetrahedra present a formidable challenge in understanding their self-assembly behavior as they do not tile space. Here, we report diverse supracrystals from gold nanotetrahedra including the quasicrystal (QC) and the dimer packing predicted more than a decade ago and hitherto unknown phases. We solve the complex three-dimensional (3D) structure of the QC by a combination of electron microscopy, tomography, and synchrotron X-ray scattering. Nanotetrahedron vertex sharpness, surface ligands, and assembly conditions work in concert to regulate supracrystal structure. We also discover that the surface curvature of supracrystals can induce structural changes of the QC tiling and eventually, for small supracrystals with high curvature, stabilize a hexagonal approximant. Our findings bridge the gap between computational design and experimental realization of soft matter assemblies and demonstrate the importance of accurate control over nanocrystal attributes and the assembly conditions to realize increasingly complex nanopolyhedron supracrystals.

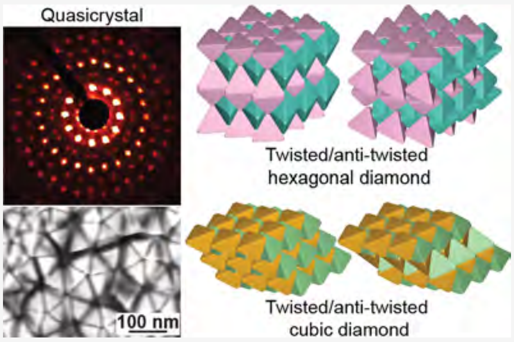

## INTRODUCTION

Tetrahedral symmetry commonly exists in chemistry and physics. It is the most common coordination geometry in organic molecules, linked to the anomalous properties of liquid water,[1] and dominates the local structure in many block copolymer mesophases and, by duality, metallic alloys.[2] Ordered assemblies of tetrahedral building blocks have been studied in diverse soft matter systems.[3−5] As a building block, the regular tetrahedron is the simplest Platonic solid yet exhibits a surprisingly rich phase behavior. Computer simulations predicted that a fluid of hard tetrahedra undergoes a first-order phase transition to an entropically stabilized dodecagonal quasicrystal (QC).[6,7] Also, the densest known packing of tetrahedra is a dimer packing,[8] whereas it is inaccessible through crystallization from the fluid phase.[9]

Nanoparticle assembly is a powerful and versatile tool to develop new multifunctional materials[10] and to study the phase behavior of anisotropic building blocks, thanks to recent advances in shape-controlled synthesis of nanocrystals (NCs).[11] Whereas hard (i.e., non-interacting) spheres are a well-established model for colloidal assembly,[12,13] effects of shape anisotropy as found in hard polyhedra are largely investigated via computer simulations.[6,14−17] Colloidal crystallization of polyhedral NCs found diverse supracrystals[18−25] but is mostly limited to systems involving high-symmetry (e.g., cubic) nanopolyhedra and truncated or rounded NCs.[26−29] In particular, the experimental realization of simulation-predicted 3D assemblies of hard tetrahedra remains elusive.

The underlying challenge is multi-faceted. First, the synthesis of nanotetrahedra requires a kinetically controlled growth pathway to favor the tetrahedron shape.[30−32] For face-centered cubic metals, such a pathway is out-of-equilibrium and requires spontaneous symmetry breaking to avoid the high-symmetry octahedron shape. Second, colloidal NCs are often covered by surface ligands, which cause rounding of the effective particle shape.[26,33] Third, the ever-present interactions between colloidal NCs and the discreteness of matter at the nanoscale can lead to nonadditivity of interactions and many-body effects, which are generally not accounted for by existing theories or simulations.[34,35] Here, we overcome these challenges through the combination of precise NC synthesis, ligand engineering, and careful design of the assembly conditions.

**Received:** May 21, 2023

## EXPERIMENTAL SECTION

**Chemicals.** Hydrogen tetrachloroaurate trihydrate ($HAuCl_4 \cdot 3H_2O$, ≥99.9% trace metals basis), sodium borohydride ($NaBH_4$, 99%), L-ascorbic acid (BioXtra, ≥99.0%), hydrochloric acid (HCl, 37%), nitric acid ($HNO_3$, 70%), 11-mercaptoundecanoic acid (MUA, 95%), and tetramethylammonium hydroxide ($NMe_4OH \cdot 5H_2O$, ≥97%) were purchased from Sigma Aldrich. Hexadecyltrimethylammonium bromide (CTAB, ≥98.0%) and hexadecyltrimethyl ammonium chloride (CTAC, ≥95.0%) were purchased from TCI America. All chemicals were used as received without further purification. Ultrapure water (resistivity = 18.2 MΩ·cm at 25 °C) obtained from a Barnstead GenPure (Thermo Scientific) water purification system was used in all experiments. All glassware was cleaned with aqua regia (a mixture of HCl and $HNO_3$ in 3:1 volume ratio), rinsed thoroughly with water, and dried before use.

**Synthesis of Gold Tetrahedra.** Truncated gold tetrahedra were synthesized by using our previously reported method,[29] which was modified based on the literature.[30] Sharp-vertex tetrahedra were synthesized by using the same method with modifications. Specifically, in the first step, ~11 nm gold spheres were prepared as follows. 5 mL of 0.5 mM $HAuCl_4$ was mixed with 5 mL of 200 mM CTAB in a 20 mL scintillation vial at 27 °C, to which 0.6 mL of freshly prepared 10 mM $NaBH_4$ was quickly injected under vigorous stirring (~1500 rpm). After stirring for 30 s, the mixture was left undisturbed at 27 °C for 3 h. Separately, a growth solution was prepared by mixing 20 mL of 200 mM CTAC, 20 mL of 0.5 mM $HAuCl_4$, and 15 mL of 100 mM L-ascorbic acid solutions. After the growth solution turned colorless, 0.5 mL of the seed solution was added and the resulting solution was gently stirred for 15 min at 27 °C. Gold spheres were purified via two rounds of centrifugation at 8000 rpm for 90 min: the first time was re-dispersed into 2 mL of water, and the second time was re-dispersed into 10 mM CTAC (aq). The gold sphere solution (red color) was finally brought to an optical density (O.D.) of 2.0 at the extinction peak wavelength of ~521 nm (Figure S1) using 10 mM CTAC (aq).

In the second step, gold tetrahedra were synthesized by using gold spheres as seeds. Typically, to synthesize ~70 nm tetrahedra, 16.2 mmol (5.18 g) of CTAC, 5.4 mmol (1.97 g) of CTAB, and 210 mL of $H_2O$ were mixed under stirring at 30 °C. Once CTAC and CTAB were fully dissolved, 108 mL of 100 mM L-ascorbic acid (aq) and 2.1 mL of the above gold sphere solution were added consecutively to the mixture. Next, 180 mL of 0.5 mM $HAuCl_4$ solution was added dropwise by using a syringe pump (18 mL/h) under gentle stirring at room temperature. Afterward, the reaction mixture was left undisturbed for another 10 min. Gold tetrahedra were purified via two rounds of centrifugation at 4500 rpm for 15 min. After the first centrifugation, the nanoparticle pellets were re-dispersed into 40 mL water. After the second centrifugation, the concentrated nanoparticle suspension at the bottom of the centrifuge tube was stored for further use.

**Purification of Gold Tetrahedra by Using Depletion Attraction.** Typically, to purify 70 nm sharp-vertex gold tetrahedra via depletion attraction, 0.3 mL of the concentrated nanoparticle suspension was added to a 15 mL centrifugation tube. Next, 2.7 mL of 120 mM CTAC was added to provide the depletion attraction that favors the face-to-face contact between flat facets of tetrahedra while excluding spherical and ill-shaped impurities. This mixture was left undisturbed for ~1 h to allow for flocculation and sedimentation of tetrahedra. Afterward, the mixture was centrifuged at 500 rpm for 20 min and the supernatant was carefully removed with a pipette. The pellets at the bottom of the tube were further rinsed with 100 $\mu$L of 120 mM CTAC several times to remove any loosely adhered impurity nanoparticles. The pellets were dispersed in 0.3 mL of 20 mM CTAC (aq). The purification was repeated for a total of four times. The concentrations of CTAC used for inducing depletion attraction were 120, 115, 115, and 115 mM.

**Preparation of PS Brush-Coated Si Substrates.** As-purchased Si substrates were cleaned with oxygen plasma for 10 min. Next, 1 mL toluene solution of 15 mg/mL hydroxy-terminated polystyrene (PS-OH, Mn: 3 kDa, PDI: 1.06, Polymer Source, Inc.) was spin-coated onto the Si substrate at 2000 rpm for 45 s. Subsequently, the Si substrate was annealed at 160 °C under vacuum for 45 h to promote the dehydration reaction between the hydroxy group of PS-OH and the silanol groups at the Si substrate. Afterward, unbound PS-OH was removed by rinsing repeatedly with toluene followed by sonication in a toluene bath for 40 min.

**Functionalization of Gold Tetrahedra with MUA.** To functionalize the gold tetrahedra with MUA, the CTAC concentration of the tetrahedron stock solution was reduced to 0.2 mM via two rounds of centrifugation at 2500 rpm each for 10 min. Afterward, the nanoparticle concentration was brought to O.D. = 100. Separately, an aqueous solution of MUA was prepared by adding 1.5 mg of MUA to 0.6 mL of water. 45 $\mu$L of 2.74 M $NMe_4OH$ (aq) was added to adjust pH to ~13 so that MUA became fully deprotonated (pKa of MUA = 4.85). Next, 600 $\mu$L of this MUA solution was added dropwise to 60 $\mu$L of the gold tetrahedron solution under vortexing (feeding ratio of MUA to NC is ~1 mM/O.D.). The mixture was sonicated for 10 s and then allowed to sit on a shaker (~1400 rpm) for >20 h. The MUA-capped tetrahedra were isolated via centrifugation at 2500 rpm for 10 min and re-dispersed in 60 $\mu$L of water together with 1.2 $\mu$L of 2.74 M $NMe_4OH$ (aq).

**Self-Assembly of MUA-Capped and CTAC-Capped Gold Tetrahedra.** To assemble the dodecagonal QC, 30 $\mu$L of the MUA-capped tetrahedra was mixed with 270 $\mu$L of water and centrifuged at 2500 rpm for 10 min. Afterward, 290 $\mu$L of the supernatant was carefully removed and the nanoparticle pellets were diluted with 10 $\mu$L of water. This solution was then drop-casted onto a polystyrene (PS) brush-coated Si substrate inside a Teflon well ($1.5 \times 1.5 \times 1$ cm$^3$). The Teflon well was quickly covered with a glass slide to slow down solvent evaporation. A typical drying time was ~30−50 h.

To assemble periodic supracrystals from MUA-capped tetrahedra, the same deposition procedure was used except that a piece of unmodified Si substrate (<100> oriented) was used. All Si substrates were cleaned by sonication in an isopropanol bath for 40 min and dried before use.

To assemble periodic supracrystals from CTAC-capped tetrahedra, a gold tetrahedron solution containing 2 mM CTAC was prepared by diluting the stock solution (in 20 mM CTAC) with water. The nanocrystal concentration was brought to O.D. = 150 prior to sample deposition. To form periodic supracrystals, 20 $\mu$L of the gold tetrahedron solution was drop-casted onto a piece of unmodified Si substrate and left to dry in open air (typically ~1.5 h).

**Characterization.** UV−Vis extinction spectra were acquired on a JASCO V-770 UV−visible/NIR spectrophotometer with the gold tetrahedra dispersed in 20 mM CTAC (aq). Scanning electron microscopy (SEM) images were taken on a Carl Zeiss Auriga 60 FIB-SEM operated at 1.50 kV. To obtain cross-sectional SEM images, Si substrates were cut into two halves using a diamond scribe and the sample stage was tilted to 54° during image acquisition. Transmission electron microscopy (TEM) images were recorded on a JEOL JEM 1400 plus microscope equipped with a $LaB_6$ filament operated at 120 kV. High-resolution transmission electron microscopy (HRTEM) imaging, coherent nano-area electron diffraction (CNED) and high angle annular dark-field scanning transmission electron microscopy (HAADF-STEM) imaging were performed on a 300 kV JEOL JEM 3200FS TEM equipped with a Gatan 4k × 4k Ultrascan 4000 camera. Zeta potential measurements were conducted on a Zetasizer Nano-ZS system (Malvern) equipped with a He−Ne 633 nm laser.

**Focused Ion Beam (FIB) Slice-and-View Tomography.** FIB-SEM slice-and-view tomography was performed on a FEI Helios NanoLab 660 DualBeam FIB-SEM microscope. The milling series was conducted at 30 kV with a $Ga^+$-beam current of 24 pA and a nominal slice thickness of 2 nm. A total volume of 2.60 $\mu$m × 1.70 $\mu$m × 0.556 $\mu$m (278 slices) was milled close to the central region of the dodecagonal QC, perpendicular to the substrate. The cut face was imaged at 38° tilting angle with enabled tilt correction and dynamic focus. The imaging was performed at 2 kV with an electron-beam current of 100 pA using the trough-the-lens (TLD) detector in secondary electron (SE) immersion mode. Data alignment was performed by first denoising the 2D slices with the total generalized variation algorithm[36] followed by linear registration with the SIFT algorithm[37] in the silx library.

**360° Electron Tomography.** Preparation of pillar-shaped cutouts was performed on a FEI Helios NanoLab 660 DualBeam FIB-SEM microscope. The selected areas were coated with carbon using the gas injection system (GIS), cut out using a $Ga^+$ beam, and glued with carbon onto copper alloy tomography tips using the lift-out technique. Afterward, the pillars were milled down to final diameters of 250 and 500 nm using a Ga-ion beam with a current of 24 pA, operated at 30 kV.

360° electron tomography was carried out on a FEI Titan Themis[3] 60−300 TEM operated at 300 kV. Two continuous tilt series of 110° were acquired at 1° increments using a Fischione Instruments model 2050 on-axis rotation tomography holder, and the sample was manually rotated by 90° in between the tilt series. Afterward, the two tilt series were merged to obtain a full 180° tilt series, which was further aligned using the SIFT implementation of Lowe in ImageJ.[37] The tilt series of both pillars were imaged in STEM mode using both the HAADF and bright-field (BF) detectors at a semi-convergence angle of 1.2 mrad and with a camera length of 91 mm resulting in a collection range of 61−200 mrad for HAADF and 34 mrad for BF. The image resolutions of 500 nm-diameter and 250 nm-diameter pillars are 0.88 and 1.20 nm, respectively. For 3D reconstruction and further 3D analysis, the BF-STEM tilt series were first corrected for thickness dependent damping using $-\ln(I/I_0)$, where I is the measured attenuated intensity and $I_0$ is the intensity of the incident beam. The 3D reconstruction was done using the simultaneous iterative reconstruction technique (SIRT) implemented with a Python-based ASTRA toolbox[38,39] with 100 iterations. The electron tomography data was analyzed using Arivis Vision 4D (version 3.3.0).

**Transmission Small-/Wide-Angle X-ray Scattering (TSAXS/TWAXS) and Grazing Incidence Small-Angle X-ray Scattering (GISAXS).** TSAXS and TWAXS were performed at the 16-ID LiX beamline of NSLS II, Brookhaven National Lab. The X-ray beam (15.14 keV) was focused to a spot size of 5 × 5 $\mu$m. Samples were scanned at a step size of 5 $\mu$m with a typical exposure time of 1 s. TSAXS patterns were recorded with a Pilatus 1 M detector at a sample-detector distance of 3.73 m. Simultaneously, TWAXS patterns were recorded with a Pilatus 900 k detector at a sample-detector distance of 0.35 m. GISAXS was performed at the 11-BM CMS beamline of NSLS II, Brookhaven National Lab. The X-ray beam (10 keV) impinged on the sample surface at an incident angle of 0.15°. The beam size was set to 0.2 (horizontal) × 0.05 (vertical) mm. GISAXS patterns were recorded by a Pilatus 2 M detector at a sample-detector distance of 5 m with a typical exposure time of 10 s. All X-ray scattering data were analyzed by using SciAnalysis.

**Simulation Snapshots.** We analyzed snapshots of earlier simulations that reported the formation of a dodecagonal QC from hard tetrahedra.[6,7] From ref 6, we took a simulation snapshot of 13,824 tetrahedra in a cubic simulation box and use it in Figure 2b,e and Movie S4. This dataset has the advantage of being extended in all directions, which allows for reliable analysis of the stacking sequence along the 12-fold symmetry axis. From ref 7, we took a simulation snapshot of 129,600 tetrahedra in a tetragonal simulation box. This simulation box has a smaller periodicity along the direction of the 12-fold symmetry axis, and the simulations were performed at a packing fraction where liquid and QC coexist. Only the QC component was analyzed, which consists of 57,602 tetrahedra. Compared to the first dataset in ref 6, this dataset is much larger and significantly better equilibrated. It was used in Figure 2a,d, Figures S8 and S9, and Movie S3.

**Slice Visualization of Simulation Data and Comparison with Electron Tomography.** Cuts through the dataset (Figure 2c−e) were created by intersecting particles with chosen cut planes. For FIB-SEM tomography slice visualization, a cut orthogonal to the 12-fold symmetry axis reveals particles within the cut plane and slightly below caused by the excitation volume of the incident scanning electron beam during SEM imaging. We emulated this effect by fading out the particle when it is close to but below the cut plane in our visualization. Sample regions with similar local order were identified and presented in Figure 2d,e to compare FIB-SEM and STEM tomography data with simulation results.

**Calculation of Fast Fourier Transform (FFT) Patterns.** For the simulation data, we performed two-dimensional Fourier transform of the particle volumes projected onto the observation plane, which is a good approximation to the TSAXS patterns. We assumed homogeneous scattering of X-rays from all parts of nanocrystals and ignored scattering from ligands or the solvent, given the large electron density difference between gold and organic matter. This approximation only weakly affects the peak intensity of the FFT patterns but does not alter peak positions. In previous simulations of hard polyhedra, the FFT patterns were calculated by placing point scatterers at the center of each particle,[7] which was insufficient for the present study. Instead, we assumed a particle shape and considered scattering from all parts of the particle by Monte Carlo integration. We found that both the decoration of the QC tiling (Figure S8) and the exact particle shape or form factor (Figure S9) strongly influenced the relative peak intensities of the FFT pattern.

## ■ RESULTS AND DISCUSSION

**Synthesis of Quasicrystalline Supracrystals.** We synthesized single-crystalline gold nanotetrahedra bound by four $\{111\}_{NC}$ facets following previously reported seed-mediated growth methods with modifications[29,30] (Figures S1 and S2). The sharpness of nanotetrahedron vertices, which is quantified by the degree of truncation parameter $t$ defined in Figure 1a, is evident from the representative HAADF-STEM image (Figure 1b). The crude products were purified using a centrifugal force-assisted depletion-based method, which improves monodispersity and minimizes nanotetrahedron vertex corrosion at high depletant concentrations by drastically shortening the sedimentation time (Figure S1). The nanotetrahedra were post-synthetically functionalized with MUA and self-assembled via slow evaporation of an aqueous solution on a hydrophobic PS-coated Si substrate (Figure 1b). The NC surface was well-passivated by the compact and densely packed saturated alkyl chains of MUA (Table S1 and Figure S3), which maximally preserves the tetrahedral shape of NCs. Deprotonated MUA ligands provide a balance between electrostatic repulsion and van der Waals attraction to impart hard particle-like interactions.[29]

Low-magnification SEM images reveal discrete supracrystals typically adopting a disk or dome shape with diameters of several micrometers (Figure 1c and Figure S4). The top of individual supracrystals features an undulating surface, and corresponding FFT pattern suggests a 12-fold rotational symmetry, which is incompatible with ordinary periodic crystals (Figure 1d). By contrast, the side-view SEM image and corresponding FFT pattern indicate that these supracrystals are periodic along the third dimension or $z$-direction (Figure 1e). Closer examination reveals that the top surface exhibits two major structural motifs: a pentagonal bipyramid formed by five tetrahedra contacting face-to-face and a hexagonal antiprismatic ring formed by 12 tetrahedra (Figure 1f). The rings stack periodically into logs, which are separated by interstitial tetrahedra (Figure 1g and Figure S5).

**Complete Structural Characterization of QC and Comparison with Monte Carlo Simulations.** The global structural order of individual supracrystals was probed by TSAXS using microfocus X-ray beams. Sharp spots with 12-fold rotational symmetry provide strong evidence for quasicrystallinity (Figure 2a and Figure S6). The presence of higher-order peaks indicates that the structural perfection persists over large length scales. The simultaneously recorded TWAXS pattern shows $(111)_{NC}$ scatterings at 30° intervals, which matches exactly the orientations of tetrahedra comprising the 12-member rings (Figure S7). To aid comparison with experimental data, we re-analyzed prior simulations of dodecagonal QC formation

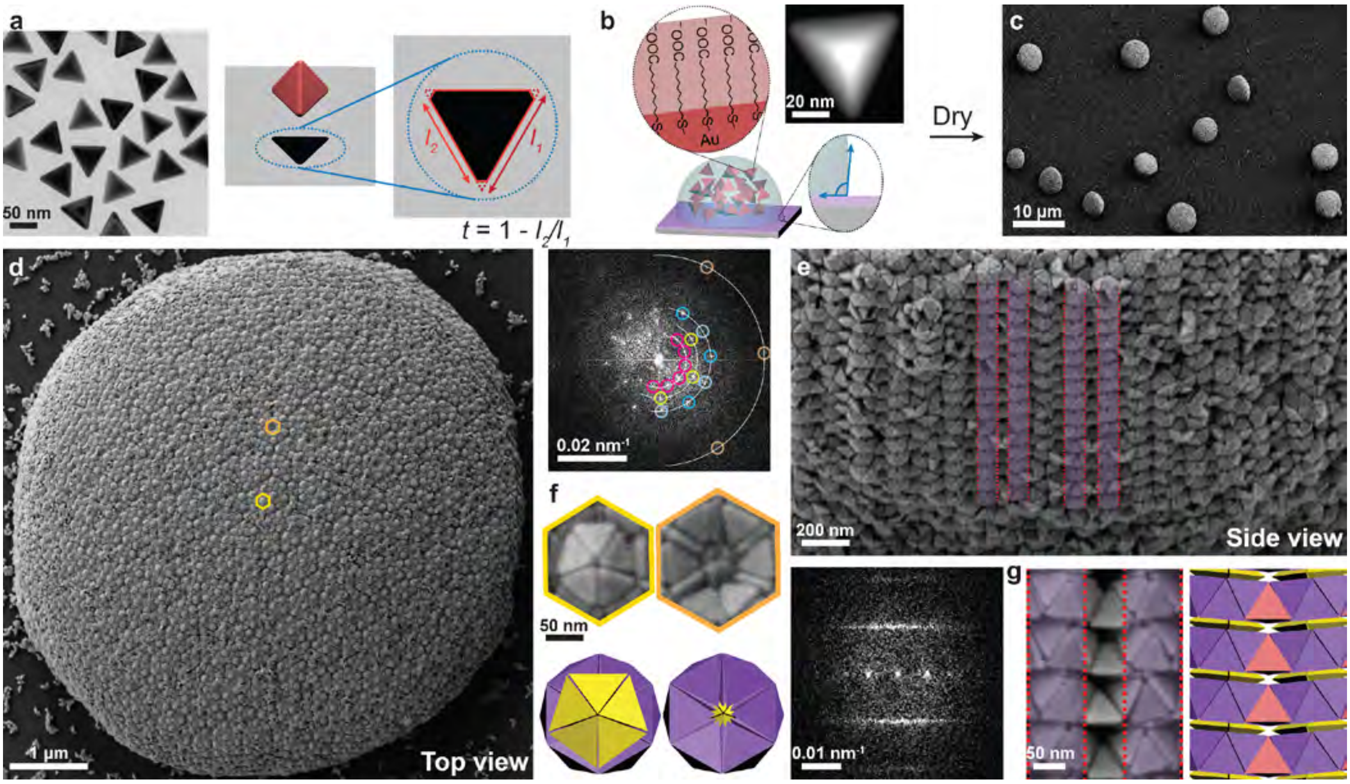

**Figure 1.** Dodecagonal QC self-assembled from gold nanotetrahedra. (a) TEM image of gold tetrahedra and schematic of a gold tetrahedron and its projection along the $<111>_{NC}$ zone axis. The degree of truncation is defined as $t = 1 - l_2/l_1$ with measured edge length $l_2$ and extrapolated edge length $l_1$. (b) Schematic illustration of drying-mediated self-assembly on a hydrophobic substrate and HAADF-STEM image of a single gold tetrahedron. Gold tetrahedra are functionalized with MUA and negatively charged. (c) Low-magnification SEM image of discrete quasicrystalline supracrystals, which are typically disk- or dome-shaped. (d,e) SEM images and corresponding FFT patterns of the QC imaged (d) along the 12-fold axis (top view) and (e) nearly orthogonal to the 12-fold axis (side view). (f,g) High-magnification SEM images and local structural motifs of the QC imaged (f) parallel to and (g) nearly perpendicular to the 12-fold axis. The images in (f), which correspond to the regions highlighted by the yellow and orange hexagons in (d), show the logs with and without a pentagonal bipyramid on top. Purple overlays in (e) and (g) denote the logs.

from hard tetrahedra.[6,7] Calculated FFT patterns of the simulation model taking into account the particle shape as form factor agree with the experimental TSAXS patterns and largely reproduce the peak positions (Figure 2a,b). Intriguingly, the calculated FFT patterns exhibit strong dependence on the tile decoration and the degree of tetrahedron truncation (Figures S8 and S9). The best agreement with the TSAXS pattern was achieved by tetrahedra whose edge and vertex truncations resemble closely the experimental NC shape. An inner ring of peaks visible in some TSAXS patterns, partially blocked by the beam stop, can be explained by excess pentagonal bipyramids at the supracrystal surface (Figure S8). On the other hand, the TSAXS pattern taken orthogonal to the 12-fold axis shows equidistant horizontal lines, which indicates a periodic arrangement along the *z*-direction (Figure 2b).

To resolve the internal structure of the QC composed of high-electron-density gold NCs, we performed FIB-SEM tomography and STEM tomography reconstructions with spatial resolution down to about 1 nm. FIB-SEM tomography provides a large lateral field of view of the supracrystals and generates high-contrast images, which allows for easy segmentation of individual nanotetrahedra.[40] Additionally, 360° STEM tomography reveals structural details at increased depths. The combination of both tomography methods enables a full 3D structural analysis of densely packed NC supracrystals. Multiple slices of the 3D reconstructed volumes from FIB-SEM tomography were selected and compared with simulation snapshots to identify similar local structures (Figure 2c−f). Despite the structural complexity, the reconstructed 3D structures match closely the model from simulations (for better visualization, see Movies S1−S7). The NC positions and orientations were revealed through five slices across half a *z*-periodicity with roughly equal spacings (Figure 2d). Two pentagonal bipyramids sit above and below each 12-tetrahedra ring. The triangle tiles are formed by three 12-tetrahedra rings plus one central tetrahedron that has two possible orientations when viewed along the 12-fold axis (face-up and vertex-up). The square tiles consist of four 12-tetrahedra rings enclosing five interstitial tetrahedra. These five tetrahedra are arranged so that the outer four form face-to-face contacts with the center one. Also, 360° STEM tomography was performed on a pillar-shaped cutout from the center region of a quasicrystalline supracrystal (Figure 2e). The reconstructed slices reveal a periodic arrangement of alternating pentagonal bipyramids and 12-tetrahedra rings along the 12-fold axis (Figure 2e), which was confirmed by the volume-rendered 3D reconstruction extracted from the FIB-SEM tomogram (Figure 2f and Movie S8). Furthermore, quantitative comparison shows that the lattice parameters retrieved from tomography reconstructions and TSAXS analyses are in excellent agreement (Figures S10 and S11).

**Formation Mechanism and Experimental Phase Diagram of Nanotetrahedron Supracrystals.** We postulate that assembly conditions and NC interactions play a critical role

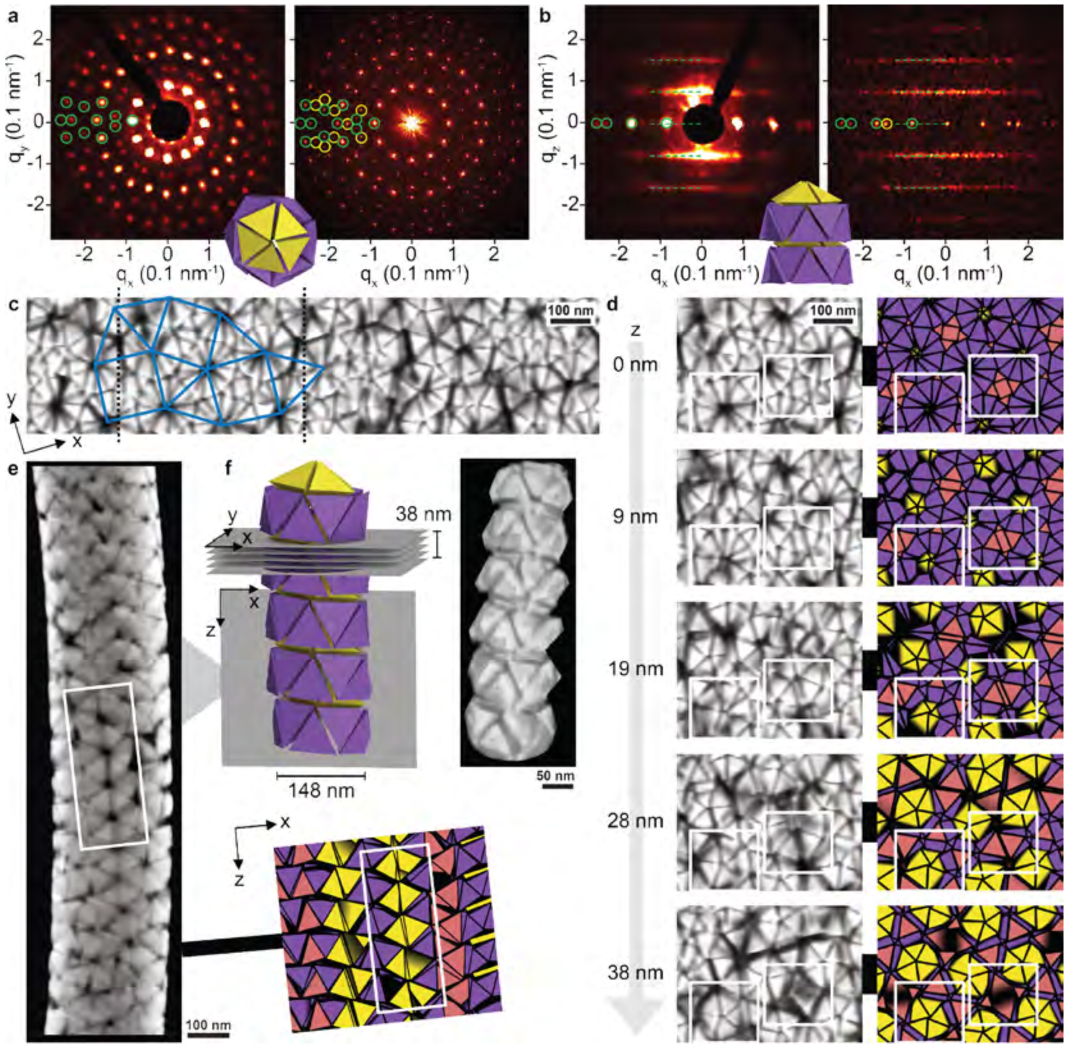

**Figure 2.** FIB-SEM tomography, electron tomography, and synchrotron X-ray scattering characterization of the dodecagonal QC. (a,b) Representative TSAXS patterns (left) and calculated FFT patterns of the simulation data (right) viewed along the 12-fold axis (a) and orthogonal to the 12-fold axis (b). Green and yellow overlays denote common diffractions between TSAXS and FFT patterns and extra spots observed in FFT patterns, respectively. Insets show the orientation of logs that consist of 12-tetrahedra rings (purple) separated by 5-tetrahedra pentagonal bipyramids (yellow). (c) Slice visualization of FIB-SEM tomography reconstruction data and square-triangle tiling analysis (see Movie S1). (d) FIB-SEM tomography slices (left) along the 12-fold axis and cuts through the simulation dataset (right) are compared at five different heights. Slice at $z = 0$ corresponds to the region between black-dotted lines in (c). (e) STEM tomography reconstruction of a 250 nm-diameter pillar sample prepared by FIB lift-out from the central region of a QC (see Movie S5). The periodic stacking along the 12-fold axis is confirmed by comparing the STEM tomography slice (left) and a cut through the simulation dataset (right). (f) (left) Schematic depiction of the orientations of cut planes (gray) in (d) and (e) on a log and (right) volume rendering of the FIB-SEM tomography reconstruction (see Movie S8).

in driving QC formation from sharp-vertex gold nanotetrahedra. A recurring structural unit involved in QC nucleation predicted by simulation is the 22-tetrahedra cluster, which consists of two pentagonal bipyramids sandwiching a 12-member ring.[7] Because this cluster is non-flat, it is incompatible with the flat Si substrate but can become favorable for homogeneous nucleation in solution without any templating effect from the substrate. One piece of experimental evidence supporting this hypothesis is the lack of a preferred orientation of various QCs with respect to the Si substrate as shown by GISAXS measurements (Figure S12). By contrast, nearly flat tetrahedron bilayers likely prefer to grow from a hydrophilic Si substrate with low contact angles at the solution-substrate interface and thus promoting the formation of periodic polymorphs.

To understand the role of substrate hydrophobicity in QC formation and to understand the phase behavior of gold nanotetrahedra as a function of important parameters like vertex sharpness and NC interactions, we synthesized a library of nanotetrahedra with $t$ ranging from 0.17 to 0.37 and performed assembly experiments under three conditions: drying over hydrophilic substrates with or without the depletants CTAC micelles and drying over hydrophobic substrates (Figure 3a−d and Figures S13−S15). Heterogeneous (homogeneous) nucleation of supracrystals was induced by self-assembly on a hydrophilic (hydrophobic) substrate that attracts (repels) the NCs at the solution-substrate interface. Besides the QC, two hexagonal diamond (HD) variants and two cubic diamond (CD) variants were obtained via assembly of weakly truncated nanotetrahedra ($t < 0.28$) on hydrophilic substrates in the presence and absence of depletants, respectively (Figure 3e−n and Figure S16). These four periodic supracrystals feature stacking of bilayers that consist of two interdigitating and

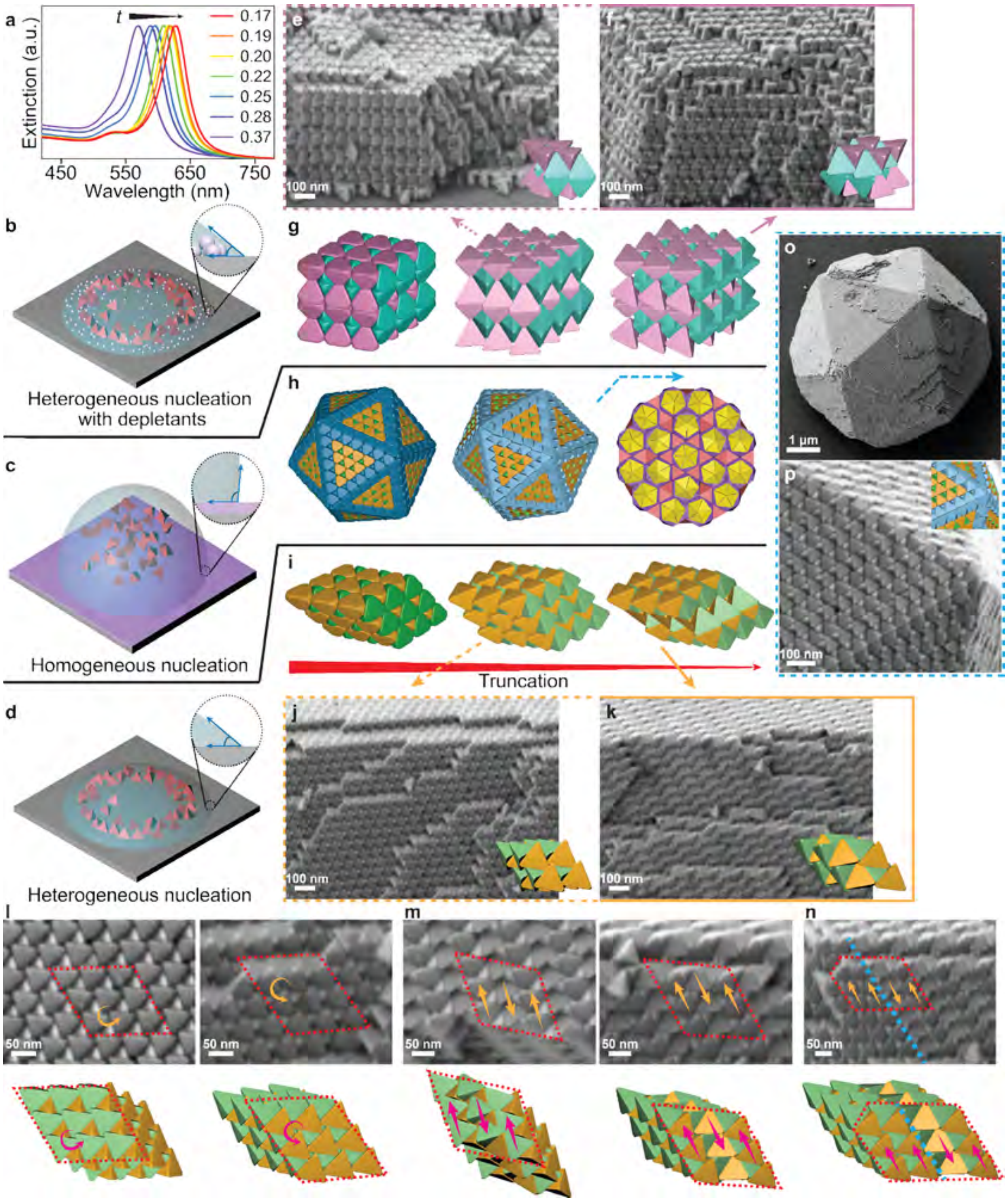

**Figure 3.** Experimental phase diagram of gold nanotetrahedron supracrystals. (a) UV−Vis extinction spectra of gold tetrahedra with varying degrees of truncation. (b−d) Schematics of drying-mediated self-assembly on (b) a hydrophilic substrate in the presence of depletants, (c) a hydrophobic substrate, and (d) a hydrophilic substrate without depletants. (e,f) Representative SEM images of (e) t-HD and (f) a-HD supracrystals. (g−i) Structural models of (g) (from left to right) HD, t-HD, and a-HD; (h) IC, t-IC, and dodecagonal QC; (i) CD, t-CD, and a-CD. (j−n) Low-magnification (j,k) and high-magnification (l−n) SEM images of (j,l) t-CD, (k,m) a-CD, and (n) the grain boundary (denoted by the blue-dotted line) between t-CD (left) and a-CD (right). (o,p) Representative low-magnification (o) and high-magnification (p) SEM images of a single t-IC. All structural models are presented with orientations matching those in the SEM images.

oppositely oriented monolayers of tetrahedra. The twisted hexagonal diamond (t-HD) phase represents a simple modification to HD through in-plane (i.e., orthogonal to the 6-fold axis) lattice compression and rotation of all tetrahedra either clockwise or anti-clockwise (Figure 3e and Figure S17). This structure has flat bilayers, which are well adapted to the geometric constraints imposed by the hydrophilic flat Si substrates. The t-HD phase also contains dimers of face-overlapping tetrahedra, making it favorable when attractive depletion interactions are present. By contrast, the anti-twisted hexagonal diamond (a-HD) phase features adjacent bilayers twisting in opposite directions and has slightly non-flat layers (Figure 3f and Figure S18). This arrangement results in minor offsets between the face-overlapping tetrahedra of a dimer and allows particles to pack denser. We reason that a-HD may become more stable than t-HD with less truncated nanotetrahedra where vertex contacts can be minimized. Furthermore, twisted cubic diamond (t-CD) deviates from the CD structure in that all tetrahedra undergo the same twisting, first parallel and then perpendicular to the 3-fold axis (Figure 3j,l and Figure S19). Similar to a-HD, the anti-twisted cubic diamond (a-CD) phase is characterized by adjacent tetrahedron bilayers

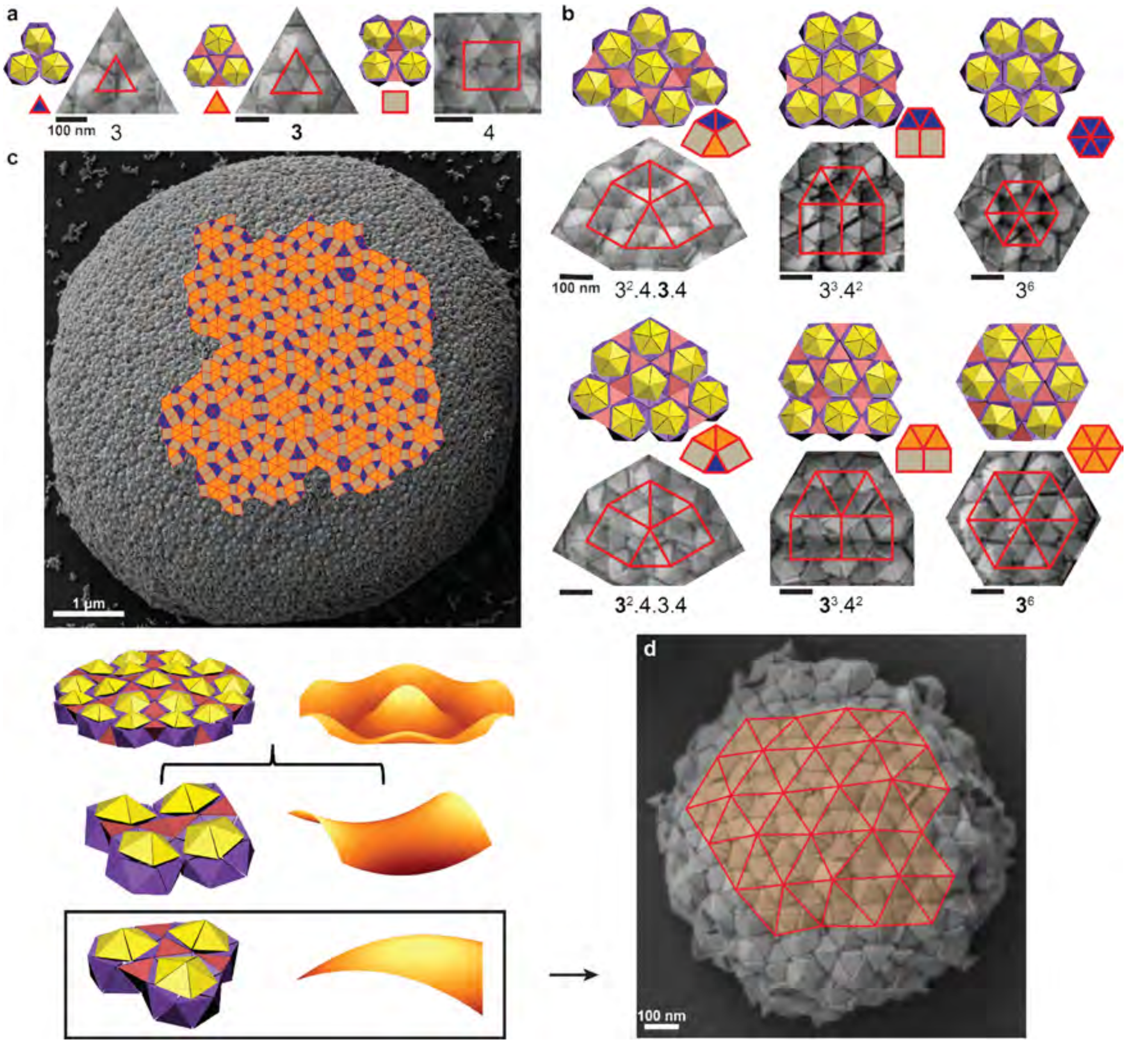

**Figure 4.** Surface tiling analysis of the dodecagonal QC and QC approximant. (a,b) Structural models, SEM images, and corresponding overlays of (a) three types of primitive tiles (from left to right): concave triangle, convex triangle, and rectangle and (b) different surface tiling motifs of the QC. The tiles are constructed by connecting the centers of pentagonal bipyramids identified from SEM images. The vertex configuration symbol is shown below each SEM image. (c,d) SEM images of (c) a QC and (d) a QC approximant overlaid with surface tile decorations. (c) Schematic illustration of surface curvatures of the QC (close-to-zero), the rectangle tile (negative Gaussian curvature), and the triangle tile (positive Gaussian curvature).

twisting in opposite directions and adopts an ABC rhombohedral stacking (Figure 3k,m and Figure S20). In fact, both t-CD and a-CD are dense packings of sharp-vertex hard tetrahedra.[41,42] They both have tetrahedron bilayers as building blocks and occasionally co-exist as nearby domains separated by well-defined grain boundaries (Figure 3n and Figure S21). The more complex stacking sequence of a-CD can better avoid the tetrahedron vertex from hitting its neighbors and thus is more stable than t-CD for less truncated tetrahedra. The structural models of the four periodic supracrystals were equilibrated by Monte Carlo simulation (Figures S22 and S23 and HTML visualization). Using nanotetrahedra with intermediate truncations ($0.25 < t < 0.28$), twisted icosahedral clusters (t-IC) consisting of 20 t-CD- or a-CD-type domains were obtained via homogeneous nucleation on a hydrophobic substrate (Figure 3o,p). Highly truncated ($t > 0.32$) nanotetrahedra crystallize into HD, icosahedral cluster (IC),[43] and CD under assembly conditions of heterogeneous nucleation with depletants, homogeneous nucleation, and heterogeneous nucleation, respectively.[29]

**Curvature-Dependent Stability of QC and Its Approximant.** We further examined different-sized QCs and identified a hexagonal QC approximant in small supracrystals (Figure 4). To understand the origin of the approximant, we constructed surface tilings on SEM images by mapping the centers of pentagonal bipyramids onto three primitive types of tiles: concave triangle (vertex configuration "3"), convex triangle ("3"), and rectangle ("4") (Figure 4a and Figure S24). The presence of two distinct triangle tiles and the appearance of rectangle tiles rather than square ones are caused by tilting of pentagonal bipyramid centers away from the log center.[6] Six common tiling motifs with well-defined vertex configurations were identified (Figure 4b and Figure S25). Crucially, preferential face-to-face contacts between the 12-tetrahedra rings and interstitial tetrahedra induced positive and negative Gaussian curvatures in triangle and rectangle tiles, respectively (Figure 4c). Minimizing the global net curvature requires both tiles and thus favors the formation of the dodecagonal QC. Intriguingly, we found an asymmetry in the occurrence frequency of tiling motifs not expected for an ideal QC tiling. For example, $3^6$ appeared more frequently than $3^6$. Given that the two types of triangle tiles are equivalent in the bulk, i.e., the **3** tile becomes the 3 tile when viewed from the other direction, the observed asymmetry could originate from the curved surface of the QCs. To confirm this hypothesis, we analyzed surface tilings of different-sized QCs. Indeed, the asymmetry becomes more pronounced as the volume of the supracrystal shrinks corresponding to increasing surface curvatures (Figures S26 and S27). For ultra-small supracrystals, the tiling consists of only convex triangles and corresponds to a hexagonal QC approximant (Figure 4d). The correlation of supracrystal surface curvature with the occurrence frequency of various tiling motifs offers important insights into particle dynamics during QC formation.

## CONCLUSIONS

In summary, we demonstrated the rich self-assembly phase behaviors of monodisperse, sharp-vertex gold nanotetrahedra. Both quasicrystalline and exotic periodic supracrystals were realized through meticulous control of NC surface chemistry and the assembly environment such as substrate hydrophobicity. Comprehensive 3D structural analyses revealed that the QC and the dimer packing match all predictions by previous computer simulations of hard tetrahedra. We further observed additional periodic supracrystals for assembly conditions that favor heterogeneous nucleation and in the presence of depletants. Finally, we discovered that the interplay between QC tilings and the surface curvature of the supracrystal can introduce phason strain, which stabilizes a hexagonal QC approximant. We expect that the assembly methods and the comprehensive 3D structural characterization demonstrated here on gold nanotetrahedra can be applied to other nanoparticles. This study thus provides a roadmap for raising the level of complexity in systems of nanopolyhedra and motivates future investigations into the formation pathways of unconventional supracrystals using in situ techniques.[25,44−47]

## ASSOCIATED CONTENT

### Supporting Information

The Supporting Information is available free of charge at https://pubs.acs.org/doi/10.1021/jacs.3c05299.

Section S1: Discussions on the effect of gravitational force on nanocrystal assembly; SEM, TEM, HRTEM, UV−Vis, CNED, and synchrotron X-ray scattering results; Monte Carlo simulations and FFT patterns; FIB-SEM tomography results; statistical analysis of tetrahedron edge length and degree of truncation; summary of supracrystals formed; library of surface tiling motifs and surface tiling analysis results; zeta potential measurement results; captions of Movies S1−S8 and HTML visualization (PDF)

Movie S1. FIB-SEM tomography reconstruction of the dodecagonal QC scanned from top to bottom along the 12-fold symmetry axis. The blue overlays appearing at 2−5 and 8−12 s indicate the square-triangle tiling (AVI)

Movie S2. FIB-SEM tomography reconstruction of the dodecagonal QC scanned perpendicular to the 12-fold symmetry axis (AVI)

Movie S3. Slice visualization along the 12-fold symmetry axis of the dodecagonal QC scanning through the simulation box shown in Figure S8. Six layers are visible. Although periodic boundaries were used in simulations, this visualization places tetrahedra such that their centers of mass fall within the simulation box. The non-flat layers explain why pentagonal bipyramids (yellow) do not come into view all at once (AVI)

Movie S4. Slice visualization perpendicular to the 12-fold symmetry axis of the dodecagonal QC. Periodicity along the vertical direction is clearly visible. The scan does not cover the whole simulation box (AVI)

Movie S5. Bright-field STEM tomography tilt series of the 250 nm-diameter pillar prepared by FIB lift-out from the central region of a large QC domain and corresponding 3D reconstruction scanned perpendicular to and along the 12-fold symmetry axis. The blue overlay appearing at 41−50 s indicates a triangle tile (AVI)

Movie S6. Bright-field STEM tomography tilt series of the 500 nm-diameter pillar prepared by FIB lift-out from the central region of a large QC domain (AVI)

Movie S7. Electron tomography reconstruction of the 500 nm-diameter pillar scanned perpendicular to the 12-fold symmetry axis of the QC (AVI)

Movie S8. Volume rendering of the FIB-SEM tomography reconstruction of a single log consisting of 6 repeating units visualized from all directions (AVI)

HTML visualization. Structural models of the experimentally observed periodic supracrystals obtained after equilibration in Monte Carlo simulations (ZIP)

## AUTHOR INFORMATION

### Corresponding Authors

**Michael Engel** − *Institute for Multiscale Simulation, Friedrich-Alexander-Universität Erlangen-Nürnberg, IZNF, 91058 Erlangen, Germany*; orcid.org/0000-0002-7031-3825; Email: michael.engel@fau.de

**Xingchen Ye** − *Department of Chemistry, Indiana University, Bloomington, Indiana 47405, United States*; orcid.org/0000-0001-6851-2721; Email: xingye@indiana.edu

### Authors

**Yi Wang** − *Department of Chemistry, Indiana University, Bloomington, Indiana 47405, United States*; orcid.org/0000-0003-2882-8777

**Jun Chen** − *Department of Chemistry, Indiana University, Bloomington, Indiana 47405, United States*; orcid.org/0000-0001-9173-3450

**Ruipeng Li** − *National Synchrotron Light Source II, Brookhaven National Laboratory, Upton, New York 11973, United States*

**Alexander Götz** − *Institute of Micro- and Nanostructure Research (IMN) & Center for Nanoanalysis and Electron Microscopy (CENEM), Friedrich-Alexander-Universität Erlangen-Nürnberg, IZNF, 91058 Erlangen, Germany*

**Dominik Drobek** − *Institute of Micro- and Nanostructure Research (IMN) & Center for Nanoanalysis and Electron Microscopy (CENEM), Friedrich-Alexander-Universität Erlangen-Nürnberg, IZNF, 91058 Erlangen, Germany*

**Thomas Przybilla** − *Institute of Micro- and Nanostructure Research (IMN) & Center for Nanoanalysis and Electron Microscopy (CENEM), Friedrich-Alexander-Universität Erlangen-Nürnberg, IZNF, 91058 Erlangen, Germany*

**Sabine Hübner** − *Institute of Micro- and Nanostructure Research (IMN) & Center for Nanoanalysis and Electron Microscopy (CENEM), Friedrich-Alexander-Universität Erlangen-Nürnberg, IZNF, 91058 Erlangen, Germany*

**Philipp Pelz** — *Institute of Micro- and Nanostructure Research (IMN) & Center for Nanoanalysis and Electron Microscopy (CENEM), Friedrich-Alexander-Universität Erlangen-Nürnberg, IZNF, 91058 Erlangen, Germany*

**Lin Yang** — *National Synchrotron Light Source II, Brookhaven National Laboratory, Upton, New York 11973, United States*

**Benjamin Apeleo Zubiri** — *Institute of Micro- and Nanostructure Research (IMN) & Center for Nanoanalysis and Electron Microscopy (CENEM), Friedrich-Alexander-Universität Erlangen-Nürnberg, IZNF, 91058 Erlangen, Germany*

**Erdmann Spiecker** — *Institute of Micro- and Nanostructure Research (IMN) & Center for Nanoanalysis and Electron Microscopy (CENEM), Friedrich-Alexander-Universität Erlangen-Nürnberg, IZNF, 91058 Erlangen, Germany;* orcid.org/0000-0002-2723-5227

Complete contact information is available at:
https://pubs.acs.org/10.1021/jacs.3c05299

## Notes

The authors declare no competing financial interest.

## ■ ACKNOWLEDGMENTS

Y.W., J.C., and X.Y. acknowledge support from the US National Science Foundation under grant numbers DMR-2102526 (nanocrystal synthesis) and CBET-2223453 (nanocrystal assembly and supracrystal analyses). A.G., D.D., T.P., S.H., P.P., B.A.Z., E.S., and M.E. acknowledge financial support by the German Research Foundation (DFG) within the framework of the Collaborative Research Centre 1411 ″Design of Particulate Products″ (Project-ID 416229255). The LiX beamline (16ID) at Center for BioMolecular Structure (CBMS) is primarily supported by the National Institutes of Health, National Institute of General Medical Sciences (NIGMS) through a Center Core P30 Grant (P30GM133893), and by the DOE Office of Biological and Environmental Research (KP1607011). This research used CMS beamline (11BM) of the National Synchrotron Light Source II, a US Department of Energy (DOE) Office of Science User Facility operated for the DOE Office of Science by Brookhaven National Laboratory under Contract No. DE-SC0012704. Y.W., J.C., and X.Y. thank the Indiana University Nanoscale Characterization Facility and the Electron Microscopy Center for access to instrumentation. B.A.Z. thanks Mingjian Wu (IMN & CENEM) for help with STEM tomography data acquisition and processing.

## ■ REFERENCES

(1) Smallenburg, F.; Filion, L.; Sciortino, F. Erasing no-man's land by thermodynamically stabilizing the liquid-liquid transition in tetrahedral particles. *Nat. Phys.* **2014**, *10*, 653−657.

(2) Lee, S.; Leighton, C.; Bates, F. S. Sphericity and symmetry breaking in the formation of Frank-Kasper phases from one component materials. *Proc. Natl. Acad. Sci. U. S. A.* **2014**, *111*, 17723−17731.

(3) Huang, M.; Hsu, C.-H.; Wang, J.; Mei, S.; Dong, X.; Li, Y.; Li, M.; Liu, H.; Zhang, W.; Aida, T.; Zhang, W.-B.; Yue, K.; Cheng, S. Z. D. Selective assemblies of giant tetrahedra via precisely controlled positional interactions. *Science* **2015**, *348*, 424−428.

(4) Liu, W.; Tagawa, M.; Xin, H. L.; Wang, T.; Emamy, H.; Li, H.; Yager, K. G.; Starr, F. W.; Tkachenko, A. V.; Gang, O. Diamond family of nanoparticle superlattices. *Science* **2016**, *351*, 582−586.

(5) He, M.; Gales, J. P.; Ducrot, É.; Gong, Z.; Yi, G.-R.; Sacanna, S.; Pine, D. J. Colloidal diamond. *Nature* **2020**, *585*, 524−529.

(6) Haji-Akbari, A.; Engel, M.; Keys, A. S.; Zheng, X.; Petschek, R. G.; Palffy-Muhoray, P.; Glotzer, S. C. Disordered, quasicrystalline and crystalline phases of densely packed tetrahedra. *Nature* **2009**, *462*, 773−777.

(7) Je, K.; Lee, S.; Teich, E. G.; Engel, M.; Glotzer, S. C. Entropic formation of a thermodynamically stable colloidal quasicrystal with negligible phason strain. *Proc. Natl. Acad. Sci. U. S. A.* **2021**, *118*, No. e2011799118.

(8) Chen, E. R.; Engel, M.; Glotzer, S. C. Dense crystalline dimer packings of regular tetrahedra. *Discrete Comput. Geom.* **2010**, *44*, 253−280.

(9) Haji-Akbari, A.; Engel, M.; Glotzer, S. C. Phase diagram of hard tetrahedra. *J. Chem. Phys.* **2011**, *135*, No. 194101.

(10) Lee, M. S.; Yee, D. W.; Ye, M.; Macfarlane, R. J. Nanoparticle assembly as a materials development tool. *J. Am. Chem. Soc.* **2022**, *144*, 3330−3346.

(11) Nguyen, Q. N.; Wang, C.; Shang, Y.; Janssen, A.; Xia, Y. Colloidal synthesis of metal nanocrystals: from asymmetrical growth to symmetry breaking. *Chem. Rev.* **2023**, *123*, 3693−3760.

(12) Manoharan, V. N. Colloidal matter: packing, geometry, and entropy. *Science* **2015**, *349*, 1253751.

(13) Li, B.; Zhou, D.; Han, Y. Assembly and phase transitions of colloidal crystals. *Nat. Rev. Mater.* **2016**, *1*, 15011.

(14) Torquato, S.; Jiao, Y. Dense packings of the Platonic and Archimedean solids. *Nature* **2009**, *460*, 876−879.

(15) Agarwal, U.; Escobedo, F. A. Mesophase behaviour of polyhedral particles. *Nat. Mater.* **2011**, *10*, 230−235.

(16) Damasceno, P. F.; Engel, M.; Glotzer, S. C. Predictive self-assembly of polyhedra into complex structures. *Science* **2012**, *337*, 453−457.

(17) Dijkstra, M.; Luijten, E. From predictive modelling to machine learning and reverse engineering of colloidal self-assembly. *Nat. Mater.* **2021**, *20*, 762−773.

(18) Henzie, J.; Grünwald, M.; Widmer-Cooper, A.; Geissler, P. L.; Yang, P. Self-assembly of uniform polyhedral silver nanocrystals into densest packings and exotic superlattices. *Nat. Mater.* **2011**, *11*, 131−137.

(19) Choi, J. J.; Bealing, C. R.; Bian, K.; Hughes, K. J.; Zhang, W.; Smilgies, D. M.; Hennig, R. G.; Engstrom, J. R.; Hanrath, T. Controlling nanocrystal superlattice symmetry and shape-anisotropic interactions through variable ligand surface coverage. *J. Am. Chem. Soc.* **2011**, *133*, 3131−3138.

(20) Singh, G.; Chan, H.; Baskin, A.; Gelman, E.; Repnin, N.; Král, P.; Klajn, R. Self-assembly of magnetite nanocubes into helical superstructures. *Science* **2014**, *345*, 1149−1153.

(21) Lin, H.; Lee, S.; Sun, L.; Spellings, M.; Engel, M.; Glotzer, S. C.; Mirkin, C. A. Clathrate colloidal crystals. *Science* **2017**, *355*, 931−935.

(22) Lee, Y. H.; Lay, C. L.; Shi, W.; Lee, H. K.; Yang, Y.; Li, S.; Ling, X. Y. Creating two self-assembly micro-environments to achieve supercrystals with dual structures using polyhedral nanoparticles. *Nat. Commun.* **2018**, *9*, 2769.

(23) Abelson, A.; Qian, C.; Salk, T.; Luan, Z.; Fu, K.; Zheng, J. G.; Wardini, J. L.; Law, M. Collective topo-epitaxy in the self-assembly of a 3D quantum dot superlattice. *Nat. Mater.* **2020**, *19*, 49−55.

(24) Cheng, Z.; Jones, M. R. Assembly of planar chiral superlattices from achiral building blocks. *Nat. Commun.* **2022**, *13*, 4207.

(25) Zhou, S.; Li, J.; Lu, J.; Liu, H.; Kim, J. Y.; Kim, A.; Yao, L.; Liu, C.; Qian, C.; Hood, Z. D.; Lin, X.; Chen, W.; Gage, T. E.; Arslan, I.; Travesset, A.; Sun, K.; Kotov, N. A.; Chen, Q. Chiral assemblies of pinwheel superlattices on substrates. *Nature* **2022**, *612*, 259−265.

(26) Boles, M. A.; Talapin, D. V. Self-assembly of tetrahedral CdSe nanocrystals: effective ″patchiness″ via anisotropic steric interaction. *J. Am. Chem. Soc.* **2014**, *136*, 5868−5871.

(27) Nagaoka, Y.; Tan, R.; Li, R.; Zhu, H.; Eggert, D.; Wu, Y. A.; Liu, Y.; Wang, Z.; Chen, O. Superstructures generated from truncated tetrahedral quantum dots. *Nature* **2018**, *561*, 378−382.

(28) Nagaoka, Y.; Zhu, H.; Eggert, D.; Chen, O. Single-component quasicrystalline nanocrystal superlattices through flexible polygon tiling rule. *Science* **2018**, *362*, 1396−1400.

(29) Wang, Y.; Chen, J.; Zhong, Y.; Jeong, S.; Li, R.; Ye, X. Structural diversity in dimension-controlled assemblies of tetrahedral gold nanocrystals. *J. Am. Chem. Soc.* **2022**, *144*, 13538−13546.

(30) Zheng, Y.; Liu, W.; Lv, T.; Luo, M.; Hu, H.; Lu, P.; Choi, S. I.; Zhang, C.; Tao, J.; Zhu, Y.; Li, Z. Y.; Xia, Y. Seed-mediated synthesis of gold tetrahedra in high purity and with tunable, well-controlled sizes. *Chem. − Asian J.* **2014**, *9*, 2635−2640.

(31) Xia, Y.; Nelli, D.; Ferrando, R.; Yuan, J.; Li, Z. Y. Shape control of size-selected naked platinum nanocrystals. *Nat. Commun.* **2021**, *12*, 3019.

(32) Sun, M.; Cheng, Z.; Chen, W.; Jones, M. Understanding symmetry breaking at the single-particle level via the growth of tetrahedron-shaped nanocrystals from higher-symmetry precursors. *ACS Nano* **2021**, *15*, 15953−15961.

(33) Liu, Y.; Klement, M.; Wang, Y.; Zhong, Y.; Zhu, B.; Chen, J.; Engel, M.; Ye, X. Macromolecular ligand engineering for programmable nanoprism assembly. *J. Am. Chem. Soc.* **2021**, *143*, 16163−16172.

(34) Batista, C. A. S.; Larson, R. G.; Kotov, N. A. Nonadditivity of nanoparticle interactions. *Science* **2015**, *350*, No. 1242477.

(35) Waltmann, T.; Waltmann, C.; Horst, N.; Travesset, A. Many body effects and icosahedral order in superlattice self-assembly. *J. Am. Chem. Soc.* **2018**, *140*, 8236−8245.

(36) Kazantsev, D.; Pasca, E.; Turner, M. J.; Withers, P. J. CCPi-Regularisation toolkit for computed tomographic image reconstruction with proximal splitting algorithms. *SoftwareX* **2019**, *9*, 317−323.

(37) Lowe, D. G. Distinctive image features from scale-invariant keypoints. *Int. J. Comput. Vision* **2004**, *60*, 91−110.

(38) Palenstijn, W. J.; Batenburg, K. J.; Sijbers, J. Performance improvements for iterative electron tomography reconstruction using graphics processing units (GPUs). *J. Struct. Biol.* **2011**, *176*, 250−253.

(39) van Aarle, W.; Palenstijn, W. J.; de Beenhouwer, J.; Altantzis, T.; Bals, S.; Batenburg, K. J.; Sijbers, J. The ASTRA toolbox: a platform for advanced algorithm development in electron tomography. *Ultramicroscopy* **2015**, *157*, 35−47.

(40) van der Hoeven, J. E. S.; van der Wee, E. B.; de Winter, D. A. M.; Hermes, M.; Liu, Y.; Fokkema, J.; Bransen, M.; van Huis, M. A.; Gerritsen, H. C.; de Jongh, P. E.; van Blaaderen, A. Bridging the gap: 3D real-space characterization of colloidal assemblies via FIB-SEM tomography. *Nanoscale* **2019**, *11*, 5304−5316.

(41) Damasceno, P. F.; Engel, M.; Glotzer, S. C. Crystalline assemblies and densest packings of a family of truncated tetrahedra and the role of directional entropic forces. *ACS Nano* **2012**, *6*, 609−614.

(42) van Damme, R.; Coli, G. M.; van Roij, R.; Dijkstra, M. Classifying crystals of rounded tetrahedra and determining their order parameters using dimensionality reduction. *ACS Nano* **2020**, *14*, 15144−15153.

(43) Lee, S.; Glotzer, S. C. Entropically engineered formation of fivefold and icosahedral twinned clusters of colloidal shapes. *Nat. Commun.* **2022**, *13*, 7362.

(44) Geuchies, J. J.; van Overbeek, C.; Evers, W. H.; Goris, B.; de Backer, A.; Gantapara, A. P.; Rabouw, F. T.; Hilhorst, J.; Peters, J. L.; Konovalov, O.; Petukhov, A. V.; Dijkstra, M.; Siebbeles, L. D. A.; van Aert, S.; Bals, S.; Vanmaekelbergh, D. In situ study of the formation mechanism of two-dimensional superlattices from PbSe nanocrystals. *Nat. Mater.* **2016**, *15*, 1248−1254.

(45) Weidman, M. C.; Smilgies, D. M.; Tisdale, W. A. Kinetics of the self-assembly of nanocrystal superlattices measured by real-time in situ X-ray scattering. *Nat. Mater.* **2016**, *15*, 775−781.

(46) Huang, X.; Zhu, J.; Ge, B.; Gerdes, F.; Klinke, C.; Wang, Z. In situ constructing the kinetic roadmap of octahedral nanocrystal assembly toward controlled superlattice fabrication. *J. Am. Chem. Soc.* **2021**, *143*, 4234−4243.

(47) Zhong, Y.; Allen, V. R.; Chen, J.; Wang, Y.; Ye, X. Multistep crystallization of dynamic nanoparticle superlattices in nonaqueous solutions. *J. Am. Chem. Soc.* **2022**, *144*, 14915−14922.